Journal of Catalysis **211,** 119–133 (2002)
doi:10.1006/jcat.2002.3735

Carbon Monoxide Oxidation on Nanostructured CuO_x/CeO_2 Composite Particles Characterized by HREM, XPS, XAS, and High-Energy Diffraction

Björn Skårman,*[,1] Didier Grandjean,† Robert E. Benfield,† Andreas Hinz,‡[,2] Arne Andersson,‡ and L. Reine Wallenberg*

*Department of Materials Chemistry, National Center for HREM, Lund University, Chemical Center, P.O. Box 124, SE-221 00 Lund, Sweden; †Centre for Materials Research, School of Physical Sciences, University of Kent, Canterbury, CT2 7NR, United Kingdom; and ‡Department of Chemical Engineering II, Lund University, Chemical Center, P.O. Box 124, SE-221 00 Lund, Sweden

Received February 18, 2002; revised June 10, 2002; accepted June 14, 2002

Nonstoichiometric CuO_x/CeO_2 nanocomposite particles have been synthesized by inert gas condensation (IGC) over the whole compositional range (2 to 98 at.% Cu). The composition influences greatly the formation of various nanostructures, such as core-shells. A wide range of techniques were used to characterize the catalysts: high-resolution TEM and X-ray photoelectron spectroscopy, as well as high-energy diffraction (HED) and X-ray absorption spectroscopy (XANES and EXAFS) using synchrotron radiation. Catalytic oxidation of carbon monoxide was performed on catalysts with equal specific surface area, using both a batch reactor and a fixed-bed flow reactor. X-ray absorption spectroscopy showed that copper was present as a mixture of Cu(I) and Cu(II) species ranging from ca. 36% Cu(I) in one of the fresh samples to less than 5% in the activated samples. The coordination of Cu(I) was found to be mostly linear 2-coordinate as in the model compound Cu_2O or alternatively 3-coordinate planar, while Cu(II) was found to present a mixture of tetrahedral and highly distorted octahedral coordination. EXAFS showed that both copper species were part of a very dispersed and highly disordered structure. The main chemical factors that control the activity for the oxidation of carbon monoxide are (i) the nanostructured morphology, (ii) the X-ray crystallinity as determined by HED, and (iii) the dispersion of copper at the surface. These three factors can be tailored during the IGC synthesis, but they can also change during the thermal activation. Copper ions migrate toward the particle surface and create new and highly dispersed superficial copper species/clusters, accompanied by a slight reduction of the CeO_2 surface. This favorable morphological evolution, or diminutive structural rearrangement, which was not adequately resolved by HREM, can be monitored as a shift of the light-off temperature. The wide variation in X-ray crystallinity between the catalysts can be used to quantify the processes occurring during the thermal activation. Easily reducible, high-energy surfaces of CeO_2 are better in stabilizing extremely dispersed copper species by a close synergistic interaction, which promotes a rapid change of valency and supply of oxygen.

Key Words: **ceria; copper oxide; nanocomposite; nonstoichiometry; crystallinity; amorphous; dispersion; morphology; carbon monoxide oxidation; thermal activation; inert gas condensation; HREM; XPS; EXAFS; XANES; high-energy diffraction.**

1. INTRODUCTION

Ceria is used in widely different application areas, such as electrolytes in fuel cells (1, 2), smart windows (3), and gas sensors (4), and as a support or additive in heterogeneous industrial catalysts (5, 6). It is, however, most widely known as an oxygen storage medium and thermal stabilizer in the automotive three-way catalytic converter (7, 8). The interaction of ceria with precious metals (Pd, Pt, Rh) and its effect on catalytic activity are therefore well documented (9–12). However, the ability of cerium dioxide to promote low-temperature combustion reactions on copper has attracted much attention in recent years (13–20). The interaction between a metal oxide catalyst, such as copper oxide, and the ceria support is complicated, since a variety of metal–support interactions can lead to synergistic effects and enhanced catalytic properties. Furthermore, chemical factors, such as crystal structure, oxidation state, crystallinity, morphology, and dispersion effects, which all may influence the activity of CuO_x/CeO_2 during catalysis, are poorly understood and need to be evaluated.

Copper, or copper oxide, on CeO_2 is known to be an efficient catalyst for various reactions such as the combustion of CO and methane (15, 16), the reduction of SO_2 by CO (21), the water-gas shift reaction (22), methanol synthesis (13), and wet oxidation of phenol (17, 18). It is not entirely clear how the supported copper species participate in oxidation reactions, although the ease with which oxygen vacancies are created in the support material appears to strongly influence its catalytic performance. We have

[1] To whom correspondence should be addressed. Fax: (46) 46 222 4012. E-mail: bjorn.skarman@materialkemi.lth.se.

[2] Present address: Volvo Technological Development AB, SE-405 08 Göteborg, Sweden.

0021-9517/02 $35.00

previously shown (23) that copper oxide exhibits a dramatically improved activity on CeO_2{001} surfaces compared to the dominating low-energy CeO_2{111}. This was ascribed to the superior ability of {001}-surfaces to assist the copper oxide in changing the valence and supplying oxygen. Hence, by controlling the properties of the oxygen-supplying species it would be possible to design the catalyst to feature specific oxidative properties (24).

Cerium dioxide is stoichiometric when prepared by precipitation from aqueous salt solutions and calcined at elevated temperature. Nonstoichiometric ceria (CeO_{2-x}) can be produced by exposure of CeO_2 to hydrogen or carbon monoxide but is readily reoxidized when exposed to an oxidizing atmosphere. Inert gas condensation (IGC) has been utilized to produce nonstoichiometric metal oxides by first synthesizing metallic nanometer-sized clusters followed by controlled oxidation (25–27). Besides the size-scaling effect of providing an enormous surface-to-volume ratio, nanocomposite clusters can be tailored to feature an unusual surface reactivity, such as that associated with extreme dispersion and preserved nonstoichiometry.

Previous research has shown that the nanocrystalline nonstoichiometric cerium oxide exhibits significantly improved catalytic properties at lower temperatures compared to its coarse-grained counterpart (28, 29). Incorporation of various lower-valent dopants, such as La^{3+} (28), Y^{3+} (30), $Ca^{2+}/Pb^{2+}/Nd^{3+}$ (31), and even four-valent Zr^{4+} (32), introduces structural defects (oxygen vacancies) into the ceria lattice and, thus, produces a slightly reduced ionic oxide with a preserved fluorite crystal structure. It has been shown that the relatively much smaller Cu^{2+} ions may be scarcely introduced into the ceria lattice (14, 33–35). However, copper is mostly observed to be highly dispersed between the crystallites of CeO_2 and to migrate toward the surface upon calcination, forming bulk CuO (25, 26, 28, 36). Besides the effect from the support material, the distribution of the copper species in the catalyst is strongly influenced by the preparation method.

Using the inert gas condensation technique almost any metal can be synthesized in a wide range of compositions, nanostructured morphologies, and particle sizes. The precise control of the growth parameters provides the possibility of manufacturing different nanosized features, such as various crust structures, noncrystalline oxide matrices with nanocrystallites either embedded or isolated on top, and finely dispersed clusters on larger supporting crystallites. Depending on the crystallite size and the post-oxidation treatment, the composite can show a wide variation of oxidation states of its constituent phases. A detailed description of the growth and morphology of CuO_x/CeO_2 nanocomposite catalysts that were produced by IGC over the whole compositional range (2 to 98 at.% Cu) has been published previously (37). In the present study we show that the composition and nanostructured morphology of CuO_x/CeO_2 greatly influence the combustion rate of carbon monoxide to carbon dioxide. In addition, the evolution of the nanostructure of the material during the thermal activation is shown to modify its catalytic properties.

The characterization is based on high-resolution transmission electron microscopy (HREM), energy-filtered TEM, X-ray photoelectron spectroscopy (XPS), high-energy diffraction (HED), and X-ray absorption spectroscopy (XANES and EXAFS), the latter two using synchrotron radiation. This is a powerful complementary combination of methods, combining small-area and whole-sample characterization of local structure and long-range order.

2. EXPERIMENTAL

2.1. Catalyst Synthesis

The catalyst powders of CuO_x/CeO_2 were synthesized by inert gas condensation utilizing resistive heating evaporation. Pure metallic cerium and copper granules (Kojundo Chemical Lab. Co., Ltd.) were used as source materials. The metals were placed separately in tungsten crucibles and evaporated simultaneously as described elsewhere (37). After the metals were pumped down to the UHV condition the chamber was filled with inert helium gas at low pressure. The helium gas pressure was used to control the particle size. Helium pressures of 0.5, 1.0, 5.0, and 10.0 Torr, respectively, were tested. The aerosol of the particles was transported via self-induced thermal convective flux to a cylindrical liquid N_2-cooled rotating cold finger, where it was continuously collected. After the evaporation the UHV ($<10^{-7}$ Torr) was reestablished and then slowly backfilled with oxygen to a final pressure of 1.0 Torr. The oxidized composite film was scraped off from the cold finger and characterized in this as-prepared powder form.

Three different reference catalysts were prepared in order to compare their light-off temperatures (Table 1). A Pt/CeO_2 reference was synthesized by IGC. Polycrystalline CeO_2 and TiO_2 supports were impregnated with an appropriate amount of an aqueous solution of copper nitrate (20). They were dried for 16 h at 353 K and subsequently calcined in air at 753 K for 4 h. Finally, the catalysts were ground to $<150\ \mu$m. Microcrystalline reference samples were also examined: CuO (tenorite), Cu_2O (cuprite), Cu powder, and CeO_2 from Kojundo Chem. Lab. Co., Ltd., Japan (Table 1).

2.2. Catalytic Measurements

The batch reactor. The catalyst powders were tested and compared for the conversion rate of carbon monoxide to carbon dioxide using a heated glass reactor working in batch mode. Since only a small quantity of each sample was synthesized, the batch reactor made it possible to quickly screen all the samples for their catalytic activity. To compare directly the catalytic properties associated with a specific structure or morphology, a fixed amount of

TABLE 1

Data and Catalytic Results for the Reference Catalysts and Bulk Materials

Reference	Pt/CeO_2	Cu/CeO_2	Cu/TiO_2	CeO_2	Cu	Cu_2O	CuO
Loading or purity	1.7 (% Pt)	24 (μmol Cu/m^2)	12 (μmol Cu/m^2)	99.9 (% Ce)	99.99 (% Cu)	99 (% Cu)	99.9 (% Cu)
BET area (m^2/g)	106	1.5	34	3.4	0.62	0.75	11.9
T_{50} (°C)[a]	183	178	226	ca. 380	145	221	128

[a] The light-off temperature for 50% conversion of 1.0% CO over 0.3 m^2 sample surface area.

surface area (0.3 m^2) of the catalyst was used. The temperature was kept constant at 323 ± 1 K. All gas samples were taken through a septum and were manually injected into the gas chromatograph. Further experimental details about the batch reactor can be found elsewhere (23).

The flow reactor. The light-off temperature measurements were performed using a fixed-bed flow reactor (4 mm in diameter). The reaction temperature was monitored using a glass-sheathed thermocouple that was placed at the top of the catalyst bed. The CO reaction gas (2.95 mol%) was a certified calibration gas balanced by nitrogen (AGA gas AB). Highly purified oxygen and nitrogen (AGA gas AB) were respectively used as an oxidizing gas and a diluent. The gas streams were measured with mass flow controllers (Bronkhorst) and were mixed prior to the reactor inlet. The preheated gas mixture flowed upward through the packed bed, which was fixed between a glass filter and a quartz wool.

To study the impact of the nanosized morphology on the catalytic activity, the reactor was filled with 0.3 m^2 surface area of the catalyst, which was diluted with fine quartz sand in order to avoid temperature differences and bed channelling. The reaction gas mixture was set to 1.0 mol% CO in synthetic air ($N_2 : O_2 = 4 : 1$) with a total flow of 50 ml/min, giving a flow of CO per unit surface area of catalyst (F_{CO}/A) of about 1.1×10^{-6} mol/s · m^2. The as-prepared catalysts (here referred to as *fresh*) were tested for their light-off temperature activity. After a stable conversion rate was reached at 573 K, the reactor was quickly cooled to room temperature, whereby a final light-off curve was acquired (here denoted as *activated* catalyst).

A Varian 3400 gas chromatograph equipped with a flame ionization detector was used to analyze the gas composition. The separation of the carbon oxides was accomplished at 338 K using a 2 m × 1/8-inch stainless steel column filled with Porapak N, 80/100 mesh. A second column, 4 cm × 1/8 inch, was connected in series and was filled with 2% Ni on acid-washed Chromosorb G, 80/100 mesh. This column was kept in a separate oven at 643 K and was used to convert the carbon oxides quantitatively into methane in the presence of hydrogen before the detector (23, 38). The conversion of carbon monoxide was followed over the specified time and was calculated according to

$$\text{Conversion of CO} = \frac{A_{CO_2}}{(A_{CO} + A_{CO_2})} \times 100(\%),$$

where A_{CO} and A_{CO_2} are the integrated peak areas of carbon monoxide and carbon dioxide being detected as methane, respectively.

2.3. Characterization

Several methods were used to characterize the catalysts, both as prepared and in their activated forms.

Energy dispersive X-ray spectrometry. A JSM-840A scanning electron microscope, interfaced with a Link AN10000 energy dispersive X-ray microanalysis system, was used to determine the bulk composition of the samples.

Nitrogen adsorption. The specific surface areas of the samples (S_{BET}) were obtained from a multipoint Brunauer–Emmet–Teller (BET) analysis of the nitrogen adsorption isotherm being recorded on a Micrometrics ASAP 2400 instrument. All samples were degassed at 373 K for 24 h before analysis. The catalyst samples displayed a specific surface area between 25 and 140 m^2/g (37), which was used to calculate the catalyst load in the microreactors.

High-resolution electron microscopy. The catalysts were characterized in a JEM 4000EX high-resolution transmission electron microscope. The microscope has a structural resolving power of 1.6 Å at an accelerating voltage of 400 kV and is equipped with an image intensified TV-rate camera, as well as a slow-scan CCD camera for direct digital recording. The powders were gently ground and dispersed onto carbon-film-coated copper grids (Oken Ltd., Japan) by dipping the grids into a methanol suspension of the powder.

X-ray photoelectron spectroscopy. X-ray photoelectron spectroscopy analyses were performed on a Kratos XSAM 800 spectrometer using Al $K\alpha$ radiation (1486.6 eV). The aluminum anode was operated at an accelerating voltage of 13 kV and a current of 19 mA. The residual pressure inside the spectrometer was 1.3×10^{-6} Pa, or lower. Charging effects were corrected by adjusting the C 1s peak to a position of 285.0 eV. Due to the photoreduction in the spectrometer

of the dispersed copper oxide (16, 19, 39) and noncrystalline cerium oxide (20, 40), the analysis of each sample was initiated with single scan analysis of the Cu 2p, Ce 3d, C 1s, and O 1s regions, in that order (for a total of 13 min), followed by a wide-scan analysis (5 min) between 0 and 1100 eV binding energy. The pass energy was set to 40 eV for the region scans and 80 eV for the wide-scan analyses.

High-energy diffraction. The high-energy diffraction measurements were carried out on Beamline ID15B (41) at the European Synchrotron Radiation Facility (ESRF), in Grenoble, France. The mean crystallite sizes of the CeO_2 grains were determined from line-broadening measurements using the Scherrer equation (42). Diffractograms of reference samples were acquired on CuO (tenorite), Cu_2O (cuprite), Cu (metal), and polycrystalline CeO_2 (ceria). These samples also were used as reference catalysts (Table 1). More aspects of the HED data evaluation and experiments have been published previously (37).

X-ray absorption spectroscopy. X-ray absorption data were collected on Beamline BM29 (43) of the European Synchrotron Radiation Facility in Grenoble, France, operating under beam conditions of 6 GeV and 200 mA using a Si (311) double-crystal monochromator. The monochromator was detuned on its rocking curve to approximately half of the maximum transmitted X-ray intensity to reduce the harmonic content of the beam at a minimum level. XAS signals were measured at the Cu *K* edge (8978.9 eV) in fluorescence mode using a 13-channel solid-state detector. Cu metal foil, CuO, and Cu_2O powders were used as reference samples and studied in transmission. Data were collected with acquisition times up to 60 min (5-s acquisition time/point). Samples were held at a temperature of 30 K controlled by a closed cycled helium cryostat. Appropriate amounts of fresh and activated catalyst samples were finely ground with boron nitride and pressed (5 bar) into 13-mm pellets, producing a suitable edge jump in fluorescence mode. The measurements were performed under static conditions on both the fresh and the activated samples.

Data reduction of experimental X-ray absorption spectra was performed using the program EXBROOK (44). Pre-edge background subtraction and normalization were carried out by fitting a linear polynomial to the pre-edge region and cubic splines to the post-edge region of the absorption spectrum. A smooth atomic background was obtained. EXAFS refinements were performed with the EXCURV98 package (44). Phase shifts and backscattering factors were calculated *ab initio* using Hedin–Lundqvist potentials.

Refinements were carried out using k^3 weighting in the range 3–12 $Å^{-1}$. Because no significant peaks were present above 3 Å, and to improve the quality of the signal for a quantitative analysis, the data were refined using Fourier filtering techniques with the same filter windows (0.5–3.0 Å) for all the samples to minimize systematic errors from cutoff effects. Fourier transform peaks were isolated with a gaussian window and the contribution of these groups of shells was extracted by inverse transformation.

3. RESULTS

3.1. High-Resolution Transmission Electron Microscopy

Commonly, the active phase of a catalyst is a metal with a higher density than the support. We have here a more unfavorable case, since Cu has less scattering power than Ce in Cu/Ce/O catalysts. However, by carefully scrutinizing HREM images and using energy-filtered TEM, we have shown that an adequate evaluation of the nanosized morphology can be performed. The samples are categorized into four compositional groups, A, B, C, and D, according to their copper content: low (Group A; <5%), medium (Group B; 5–25%), high (Group C; 25–70%,), and very high copper content (Group D; >70%). These groups may also serve as categories for the catalytic properties if the morphology of the sample is taken into consideration.

Group A: Samples with low copper content (<5%) generally exhibit various types of aggregates of nanosized CeO_2 crystallites. Viewed at lower magnifications (≤120 kX) the sample appears to constitute of a large portion of amorphous material. This is indicated by the rounded particle shape and continuous diffuse rings by selected area electron diffraction pattern (37). At high magnification (Fig. 1), however, it is evident that the composite particles are assembled by differently oriented, but epitaxially interfaced crystallites. Nevertheless, the lowest crystallinity factor (37)

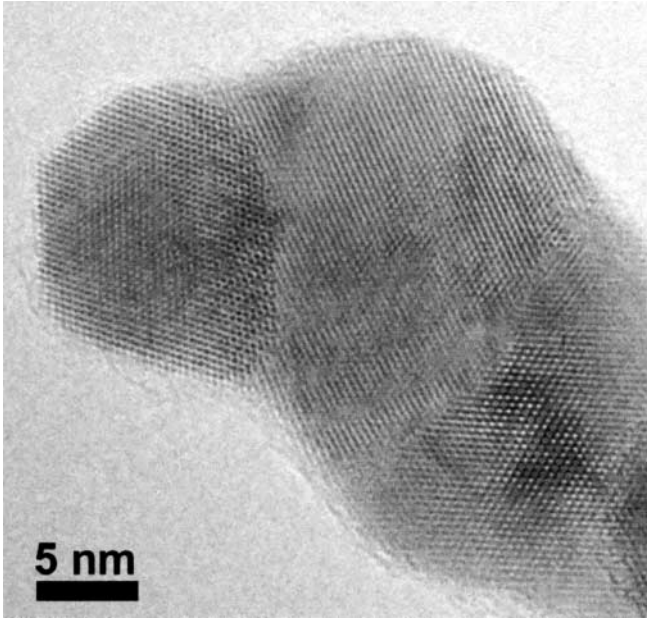

FIG. 1. The smoothly rounded particles of catalyst A4 (4.9% Cu) are shown by HREM to consist of epitaxially interfaced nanosized crystallites of ceria.

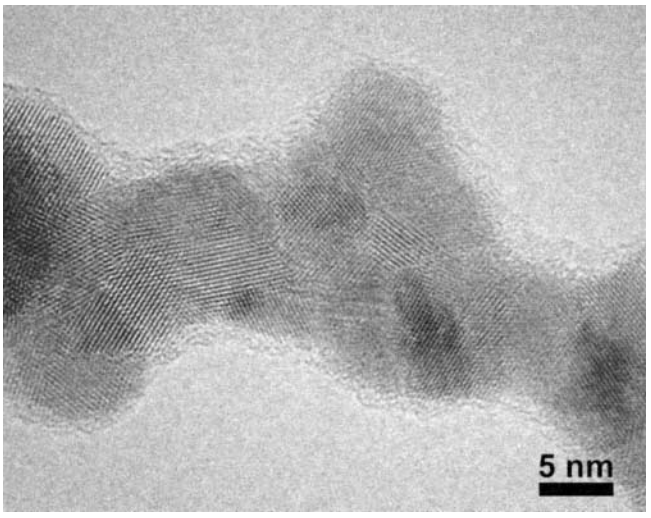

FIG. 2. HREM image of catalyst B4 (13.1% Cu). The composite particles are built up by tightly interfaced nanocrystallites, which apparently are embedded in a thin amorphous film.

was obtained for this sample, which would point out a very amorphous character consisting of poorly X-ray crystalline material.

Group B: For medium copper content (5–25%), the composite catalysts exhibit an exceptionally uniform morphology with particles of similar size. Figure 2 shows a typical HREM image of the catalyst B4 (13.1% Cu). We carefully scrutinized the HREM images by fast Fourier transform (FT) analysis but did not find any clear indications of spacing between 2.0 and 2.6 Å, which would be significant for CuO_x crystallites. The CeO_2 crystallites are evenly enveloped by a thin film, which might be an amorphous form, or very small clusters, of CuO_x. This composition range is shown here to exhibit the best catalytic activity for CO oxidation. It is worth pointing out that the catalysts in categories A and B can also be produced with a higher degree of crystallinity, displaying block-shaped particles with sharp faceted edges and flat surfaces, by carefully choosing the IGC parameters (37).

Group C: For high copper content (25–70%) the composite catalyst shows a tendency to form crust structures. Figure 3 displays a representative sample with ca. 30% Cu (C1). Exceptionally thin CeO_2 nanocrystals (~5 Å) form elongated crust structures with an apparently empty core. As previously shown by EFTEM (37) the copper seems to be evenly distributed over the ceria lattice, confirming an extremely high dispersion. A model of the formation of crust structures has been suggested previously (37). Above a 30% copper content the copper forms X-ray detectable crystals of tenorite CuO, which were not observed by TEM. The major portion of the copper, though, was found to be still highly dispersed.

Group D: For very high copper content (>70%), a few CeO_2 nanocrystallites are embedded in a generally amorphous matrix of copper oxide. Compared to the samples of category A, the sample morphology is here seemingly reversed: nanosized crystalline ceria caps are evenly distributed on an amorphous copper oxide support presenting a crystalline core (37). For samples with copper content above ca. 97%, phases composed of not fully oxidized or metallic copper were identified.

3.2. X-Ray Photoelectron Spectroscopy

For Cu-containing compounds, it is known that the intensity of the satellite peaks (at approx 943 and 963 eV binding energy) decreases with the reduction of Cu(II), since the *d* shells of Cu(0) and Cu(I) are filled and, therefore, cannot give rise to satellite peaks (43, 46, 47). Thus, the degree of reduction can be investigated by determining the ratio of the intensities of the satellite peaks to those of the principal peaks (I_{sat}/I_{pp}). Due to the photoreduction in the spectrometer (39, 46), it is difficult to estimate the accurate degree of reduction, but the method gives valuable information for comparison between catalysts. When samples were compared to a bulk CuO reference sample ($I_{sat}/I_{pp} = 0.57$), a slightly reduced copper phase was observed for all fresh catalysts (37). For activated catalysts the copper appears to be oxidized, giving higher ratio values (Table 2).

The peak intensity ratio of the copper and cerium XPS regions ("I_{Cu2p}/I_{Ce3d}") (analysis depth of <2 nm) represents a relative evaluation of the dispersed copper species over the ceria surface. Only the principal peaks Cu(II)$2p_{3/2}$

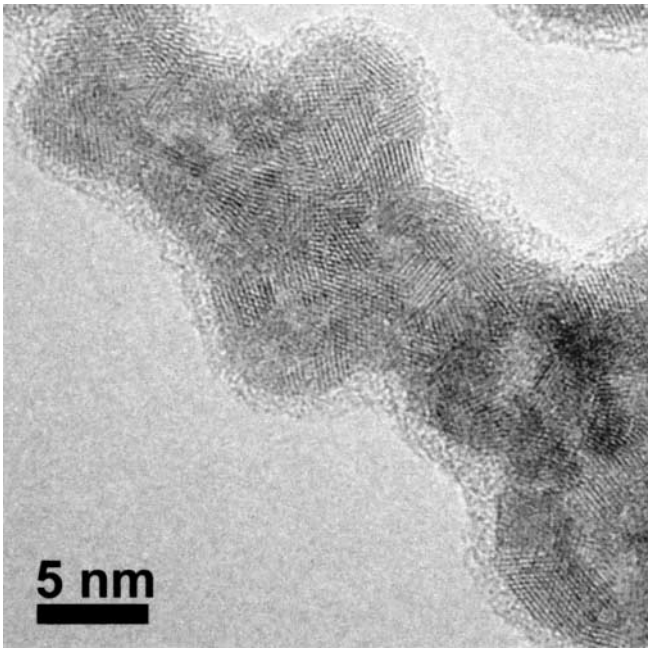

FIG. 3. HREM view of catalyst C1 (29.4% Cu) showing elongated shell structures. Nanosized crystallites of ceria form crust structures with an apparently empty core.

TABLE 2

Surface Compositional Analysis and Binding Energies of the B4 (13.1% Cu) Catalyst by XPS

	Bulk materials	Fresh catalyst	Activated catalyst
I_{Cu2p}/I_{Ce3d}[a]	3.365 (1.0)	0.333 (0.099)	0.534 (0.159)
I_{sat}/I_{pp} (Cu 2p)	0.570 (CuO)	0.286	0.367
(Ce(IV)$3d_{3/2}$)/Ce 3d(tot)	0.135 (CeO_2)	0.108	0.098
Ce(III)$3d_{5/2}$ (eV)	882.6 (CeO_2); 888.2 (CeO_{2-x})[b]	882.2	883.9
O 1s (eV)	529.3 (CeO_2); 533.8 (CeO_{2-x})[b]	529.3	530.8

[a] Ratio values of the peak areas, as well as a relative surface quantification of copper (in parenthesis).
[b] Reduced B4 catalyst (treated in 1.0% H_2 in N_2 at 473 K for 30 min).

and Ce(IV)$3d_{3/2}$ were used to avoid the variations in oxidation state. The catalyst surface was enriched in copper after activation, which is indicated by a higher I_{Cu2p}/I_{Ce3d}-ratio value. In contrast, the binding energy value of the O 1s peak is observed to increase for used catalysts, approaching the value of Cu(I) oxide (Cu_2O, 530.8 eV), or reduced ceria (CeO_{2-x}) (48). Since CeO_2 represents the major surface area of the examined samples (group B), the O 1s signal reveals predominately the characteristics of the ceria surface and thereby stands for the observed reduction of the catalyst surface. According to Shyu *et al.* (49), the fraction of the Ce(IV)$3d_{3/2}$ peak (at ~916.8 eV) to the total Ce 3d intensity depends on the Ce(III)/Ce(IV) ratio. A reduced CeO_2 surface is confirmed by a decreasing ratio, as well as a higher binding energy of the Ce(III)$3d_{5/2}$ signal (at ~882.6 eV) (Table 2). The degree of ceria reduction is increased by ca. 9% for activated catalysts, compared to fresh catalysts. Likewise for dispersed copper, one must be aware of the possibility of having a photoreduction of dispersed cerium in the spectrometer (40, 50).

3.3. High-Energy Diffraction

The high-energy X-ray diffraction patterns of the CuO_x/CeO_2 catalysts show clear evidence of the presence of the CeO_2 face-centered cubic fluorite phase (space group *Fm3m*) (37). An average unit cell expansion of ca. 0.08 vol%, relative to a microcrystalline CeO_2 reference sample ($a_0 = 0.5415$ nm) was detected for the gas-phase-produced catalysts. As expected from the HREM studies, the crystal size of ceria is anisotropic (+9.3 %), i.e., flat crystals, bounded by predominately {111} surfaces. The average crystal size was estimated to be 10 nm with a standard deviation of 2 nm. Both the crystal size and the secondary particle size of the composite can be controlled by the helium pressure during the IGC synthesis, with larger sizes associated to higher pressures (37).

Above 30% copper content, the characteristic peaks of CuO corresponding to the *d* values 2.32 and 2.53 nm begin to appear. For copper content between 30 and 97% the only X-ray detectable copper phase was the tenorite, CuO. Above ca. 97% Cu, also the Cu_2O phase (cuprite) and metallic Cu were detected (37). The fresh samples exhibit small diffraction line variations ($\beta_{2\theta}$), but without any systematic correlation to either the crystal size or the copper content.

In our previous investigation (37), a *crystallinity factor* has been defined as the fraction of the total peak intensity to the total background intensity within a specified region (I_P/I_B). The crystallinity factor has been used for the characterization of the present catalysts. However, it should be emphasized that the defined factor is quantitatively uncertain and must strictly be used for comparison between samples within a similar series of experiments only. The crystallinity factor is given in Table 3 and is observed to vary considerably between the examined catalysts. A close correlation to the nanosized morphology, as well as the behavior of the catalyst during thermal activation, will be presented below. The crystallinity factor will hereafter be referred to as the X-ray crystallinity of the catalyst.

3.4. X-Ray Absorption Spectroscopy

X-ray absorption spectroscopy techniques are able to detect the local coordination (interatomic distances and coordination numbers) around the copper ions even when they are present in very low concentrations and in phases that are amorphous to X-ray diffraction. We chose to investigate three catalysts, A4 (4.9% Cu), B4 (13.1% Cu), and C1 (29.4% Cu), in which the copper phase was not, or was just barely, detected by HED (37). It should be pointed out that the activated catalysts were recorded *ex situ*, which may reveal information different from that of a catalyst in action. Information of the oxidation state during the catalytic event may thus be somewhat distorted. Nevertheless, the changes in the environment of the copper ions can give information about what processes have occurred during the induction and/or catalytic event.

XANES analysis. Background corrected and normalized experimental XANES Cu–K spectra of the three selected CuO_x/CeO_2 composites A4, B4, and C1, each one in its fresh and activated forms, are shown in Fig. 4 along with the reference compounds CuO and Cu_2O. For the fresh catalyst samples, as well as for the Cu_2O reference sample,

TABLE 3

Light-Off Temperature Data and HED Crystallinity Factors for the Selected IGC-Produced Catalysts

Catalyst	Bulk Cu cont. (%)	BET surface area (m^2/g)	T_{50} (°C)[a]		ΔT_{10-90} (°C)[b]		T_{50} shift (°C)	Crystallinity factor (I_P/I_B)
			Fresh	Activated	Fresh	Activated		
A1	2.8	30.7	242.5	229.0	n.d.	n.d.	−13.5	0.187
A2	3.2	41.2	255.0	252.0	n.d.	n.d.	−3.0	0.259
A3	4.5	42.2	162.8	161.5	115.7	112.0	−1.3	0.290
A4	4.9	36.6	126.7	105.8	86.1	73.9	−20.9	0.051
B1	8.0	24.5	—	136.6	—	61.0	—	—
B2	11.5	52.7	152.1	131.6	72.8	67.5	−20.5	0.170
B3	13.0	39.5	111.4	111.1	96.9	98.8	−0.3	0.395
B4	13.1	58.6	117.6	109.6	63.5	61.1	−8.0	0.209
C1	29.4	59.4	128.1	102.1	72.7	33.7	−26.0	0.172
C2	54.0	55.3	127.6	111.8	78.0	55.0	−15.8	0.168
C3	68.0	111.1	138.1	112.9	54.7	55.2	−25.2	0.140
D1	84.3	76.0	—	135.3	—	38.6	—	—
D2	97.5	52.9	—	132.5	—	31.5	—	—

Note. n.d. $= T_{90}$ is above 350°C and, thus, ΔT_{10-90} is not determined.

[a] The corresponding light-off temperatures for 50% of CO conversion. The light-off curves were nicely reproduced, giving a small standard deviation on T_{50} (±0.1°C).

[b] The temperature range flanked by the 10 and 90% conversion levels of CO.

a relatively intense pre-edge at ca. 8982 eV is observed. The intensity of this peak is not correlated to the copper content of the sample. The highest intensity is observed for the catalyst that has the lowest copper content, A4, and the lowest intensity for the catalyst that presents a medium copper content, B4. The catalyst featuring the highest copper content, C1, lies in between. On the other hand, this feature is absent in the three spectra of the activated catalysts, as well as the CuO reference sample.

EXAFS analysis. Results of the EXAFS structural refinements are summarized in Table 4. The Fourier transforms, after phase correction of the $k^3\chi(k)$ EXAFS of the three catalysts A4, B4, and C1, in both their fresh and activated forms, are plotted together with the reference compounds CuO and Cu_2O in Fig. 5.

The Fourier transforms of all the catalysts exhibit, before phase correction, a main broad peak around 1.9 Å corresponding to an oxygen shell, and a much smaller peak around 2.95 Å corresponding to a copper shell (Fig. 5, Table 4). The fresh A4 sample exhibits also a shoulder on the main peak at ca. 2.43 Å corresponding to an oxygen shell that was not observed on the other samples. In all cases, the peaks corresponding to the higher copper–copper

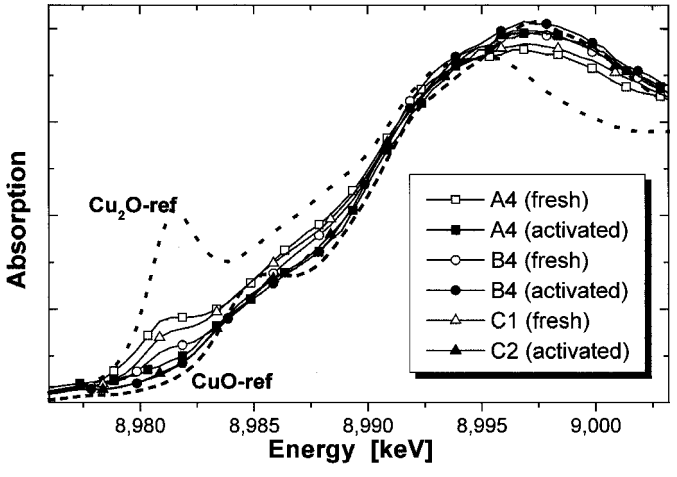

FIG. 4. Background corrected and normalized XANES spectra of three different catalysts, fresh and activated, together with CuO and Cu_2O reference samples. (Open and solid markers depict fresh and activated catalysts, respectively).

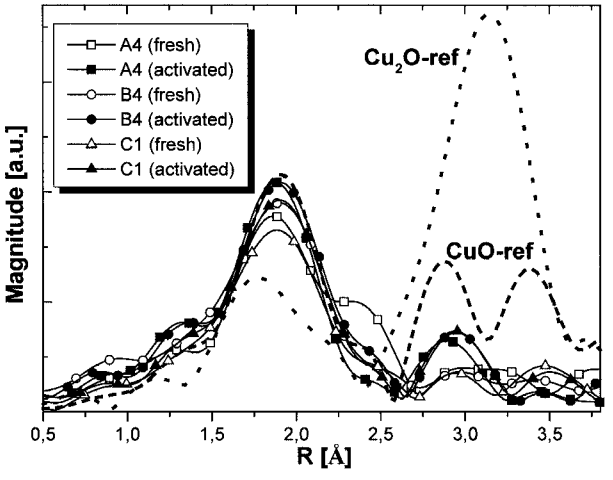

FIG. 5. Fourier transform after phase correction of the $k^3\chi(k)$ EXAFS of the three catalysts A4, B4, and C1 in their fresh and activated forms. The Fourier transforms of CuO and Cu_2O are presented as references. (Open and solid markers depict fresh and activated catalysts, respectively).

TABLE 4

Refined Structural Parameters from the Cu *K*-Edge EXAFS Data

Sample	Atom type	N	R_d	*A*	Ef	R_{factor}
Cu_2O ref.	O	2[a]	1.846[b]	0.007(1)	−9.5(3)	7.7
	Cu	12[a]	3.014[b]	0.014(3)		
CuO ref.	O	2[a]	1.958[c]	0.011(6)	−0.8(8)	11.6
	O	2[a]	1.961[c]	0.011(6)		
	O	2[a]	2.777[c]	0.029(7)		
	Cu	4[a]	2.905[c]	0.016(8)		
A4 (4.9% Cu)						
Fresh	O	3.5(2)	1.890(5)	0.015(1)	8.3(7)	10.9
	O	2.1(3)	2.479(3)	0.001(2)		
	Cu	3(1)	2.89(1)	0.05(1)		
Activated	O	3.7(4)	1.943(4)	0.005(2)	1.3(9)	13.6
	Cu	2.3(7)	2.864(7)	0.019(4)		
B4 (13.1% Cu)						
Fresh	O	4.1(4)	1.924(6)	0.01(2)	4.7(8)	17.3
	O	2(1)	2.48(3)	0.03(3)		
	Cu	0.9(7)	2.89(3)	0.03(2)		
Activated	O	3.8(2)	1.923(5)	0.008(1)	6.0(8)	16.5
	O	2(1)	2.49(2)	0.02(2)		
	Cu	0.8(4)	2.849(8)	0.008(6)		
C1 (29.4% Cu)						
Fresh	O	3.8(4)	1.924(7)	0.009(2)	1.9(9)	20.3
	Cu	0.4(4)	2.85(2)	0.01(1)		
Activated	O	3.7(3)	1.935(5)	0.008(2)	1.9(7)	16.1
	Cu	1.1(4)	2.866(9)	0.09(6)		

Note. Ef, contribution of the wave vector of the zero photoelectron relative to the origin of *k* [eV]. R_d, radial distance of atoms (Å). A, Debye–Waller term of the different shells ($A = 2\sigma^2$ with σ = Debye Waller factor) (Å^2). R factor in %.

[a] These coordination numbers were kept fixed during the fit.

[b] Cu_2O cell parameter $a = 4.262(3)$ (Å).

[c] CuO cell parameter $a = 4.70(2)$, $b = 3.42(3)$, $c = 5.13(4)$ (Å).

or copper–oxygen distances in the reference samples CuO and Cu_2O are very much suppressed or even absent in the FT of the different catalysts.

The result of the refinement shows that all the catalysts present a first coordination shell composed of 3.5 to 4.1 oxygen atoms at a distance ranging from 1.89 to 1.94 Å. A second oxygen shell composed of two oxygen atoms at a distance of ca. 2.48 Å could only be fitted for half of the six samples. In this case, the very high Debye–Waller factors associated with this shell (except for A4) indicate the presence of great disorder. Finally, all the data could be fitted with a copper shell at a distance varying from 2.89 to 2.85 Å corresponding to a very low coordination number (between 0.4 and 3). This shows that the copper is very dispersed and does not form a proper crystalline structure, which is corroborated by the HED study.

3.5. Carbon Monoxide Oxidation

Batch reactor results. Figure 6 shows the variation of the carbon monoxide oxidation rate over various CuO_x/CeO_2 powder catalysts exposing an equal specific surface area (0.3 m^2). The reported conversion rates were acquired reproducibly after the thermal activation, i.e., after the catalysts had reached stable working activities at 423 K.

The catalysts in group A (<5% Cu) display generally a poor catalytic activity, whereas the highest conversion rates were obtained for group B catalysts (5–25% Cu content). For higher copper content, above 25% (group C), the conversion rate is reduced compared to the group B catalysts.

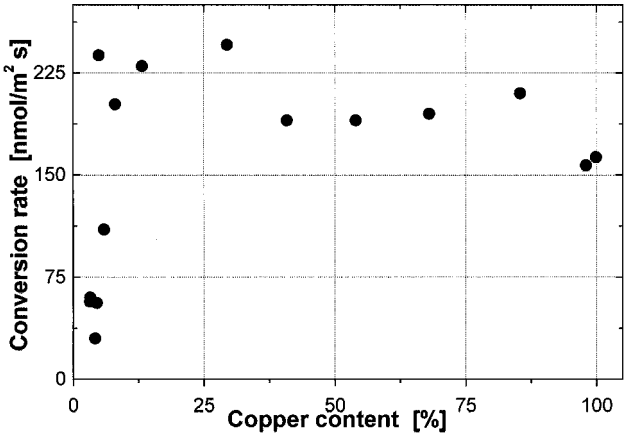

FIG. 6. The variation of the conversion rate for the oxidation of carbon monoxide with the bulk copper content. The data were acquired in a batch reactor at 423 K over 0.3 m^2 of catalyst surface area. The initial gas composition was 1.0% CO in synthetic air.

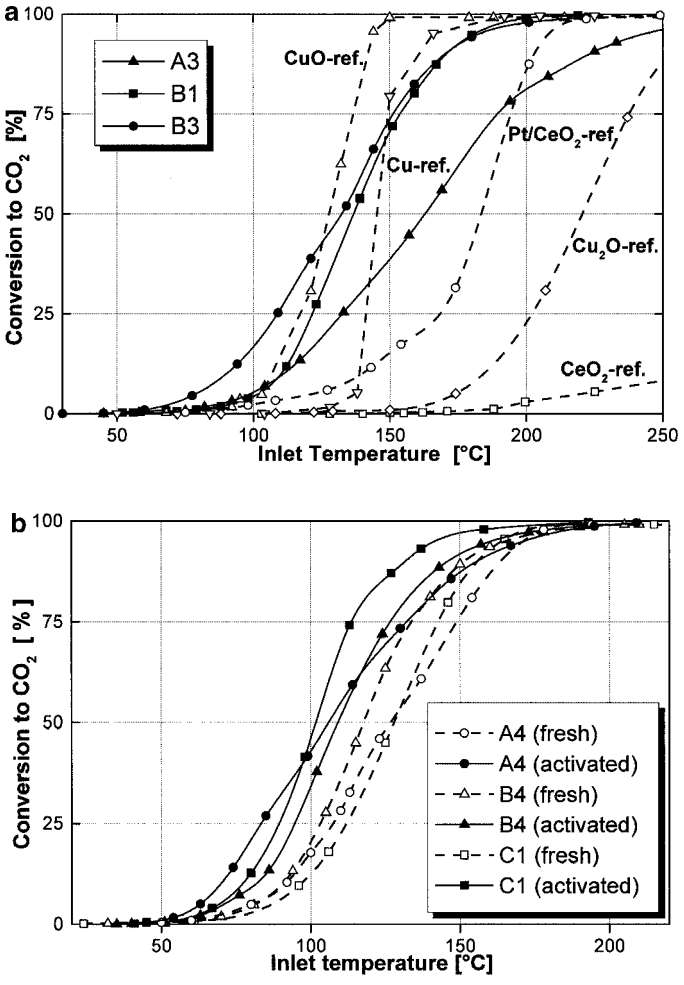

FIG. 7. (a) Light-off temperature results for the combustion of carbon monoxide in the plug flow reactor. Miscellaneous CuO_x/CeO_2 catalysts and reference samples. For notation see Tables 3 and 1, respectively. The composition of the feed gas was 1.0% CO in synthetic air, giving a flow of CO per unit surface area of about 1.1 μmol/s $\cdot$ m^2. (b) Light-off temperature results for the combustion of carbon monoxide in a plug flow reactor over 0.3 m^2 of catalyst surface area. A selection of the most active CuO_x/CeO_2 catalysts (open and solid markers depict fresh and activated catalysts, respectively). For notation see Table 3. The feed gas composition was 1.0% CO in synthetic air, giving a flow of CO per unit surface area of about 1.1×10^{-6} mol/s $\cdot$ m^2.

At around 80% Cu the conversion rate is slightly improved and shows the maximum conversion rate for the group C and D catalysts.

Light-off temperature results. Figures 7a and 7b display the light-off temperature results for the combustion of 1.0% CO in synthetic air on the CuO_x/CeO_2 catalysts, as well as on the reference samples. Data corresponding only to a selection of the examined catalysts (a total of 40 samples) which best illustrate the catalytic differences are presented. The corresponding light-off temperatures for 50% (T_{50}) of CO conversion, as well as the temperature range, flanked by the 10 and 90% conversion levels (ΔT_{10-90}) of CO, are presented in Table 3.

The pure microcrystalline CeO_2 reference sample displays only 10% conversion of CO to CO_2 at 250°C and is therefore considered relatively inactive (Fig. 7a, Table 1). For low copper content (<5%) the shape of the CO light-off temperature curve resembles that for pure CeO_2; i.e., the temperature window between the starting and the ending points (at 100% CO_2) of the conversion is relatively wide. For catalysts with higher copper content the conversion curve shows gradually a steeper slope, which is also demonstrated by the decreasing ΔT_{10-90} values (Table 3).

CuO_x/CeO_2 catalysts displaying a uniform particle size distribution exhibit higher catalytic activities than catalysts showing a particularly wide particle size distribution. A typical catalyst sample of the latter is displayed in Fig. 8 (B1; 8.0% Cu). The major portion of copper is situated in larger bulk particles, which results in relatively poor catalytic activity (Fig. 7a).

By monitoring the shift of the light-off temperature toward lower temperatures as the conversion rate stabilizes, the induction processes (i.e., the processes occurring during thermal activation before the catalyst assumes its maximum activity) may be experimentally determined. Figure 9 shows the light-off temperature shift for 50% conversion, from fresh to activated catalysts, plotted versus the crystallinity factor obtained by high-energy diffraction. The T_{50}-temperature shift is shown to decrease for increasing crystallinity factors and reaches a stable level at higher crystallinity factors ($I_P/I_B > 0.3$). Hence, samples displaying an apparent amorphous character show a larger shift of the T_{50}

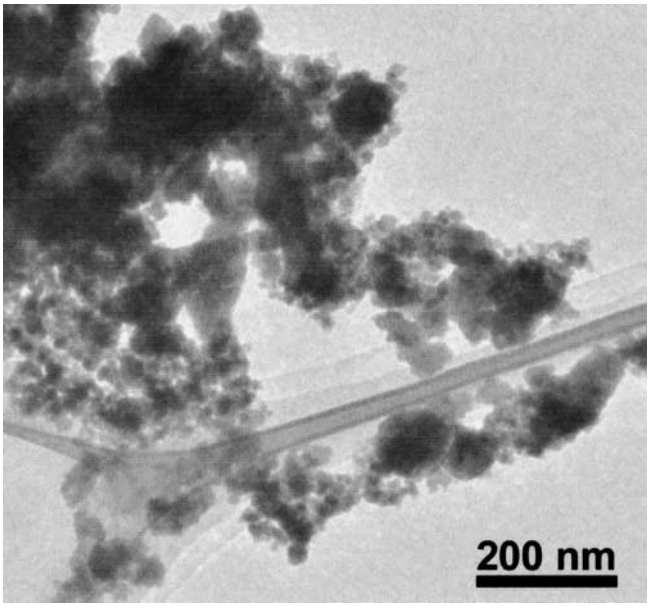

FIG. 8. A TEM image of catalyst B1 (8.0% Cu) shows a broad size distribution of particles. In spite of the optimum copper content, this catalyst shows a relatively low activity for the CO oxidation (Table 3), which is attributable to the uneven distribution of copper, situated in larger bulk particles.

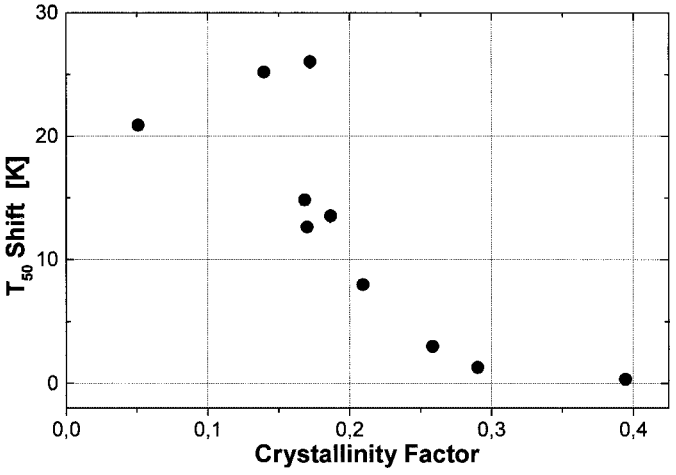

FIG. 9. The light-off shift (defined as the temperature difference between fresh and activated catalysts at T_{50}) is plotted versus the crystallinity factor (Table 3). The quantity of induction processes (i.e., evolution of nanostructure) is reduced for catalyst samples with higher X-ray crystallinity.

temperature and, consequently, require a longer induction period. The catalyst A4 (4.9% Cu) with the lowest crystallinity factor shows indeed a huge temperature shift for T_{50} (−20.9°C) (Fig. 1, Table 3). The activated A4 catalyst reaches a superior catalytic activity below ca. 40% conversion (Fig. 7b). The catalyst C1, consisting of considerably more copper (29.4%), shows similar behavior, but with a steeper curve shape due to the higher copper content.

The fresh catalyst B4 (13.1% Cu) initially displayed the lowest temperature for 50% conversion of CO to CO_2, while the light-off temperature (T_{50}) for the activated catalyst is improved by 8°C (Fig. 7b, Table 3). For this sample, the T_{50} temperature is thereby close to that of the activated B3 catalyst with a similar copper content (13.0% Cu, Fig. 7a). The catalyst B3, however, exhibits a smaller T_{50} temperature shift and a clearly wider temperature range between 10 and 90% conversion (ΔT_{10-90}).

We find that for the pure CuO (tenorite) reference the T_{50} temperature is about 17 and 93°C lower as compared to the pure Cu metal and Cu_2O references, respectively (Fig. 7a, Table 1). Thus, in agreement with other published results (53, 54), CuO is the best pure copper catalyst for CO oxidation. The pure microcrystalline reference samples (Cu, Cu_2O, CuO, CeO_2), as well as the catalysts showing the highest crystallinity factors (e.g., A2, B3), exhibit instantly a very stable light-off temperature curve.

For reasons of comparison only, we found it worthwhile to test the combustion of carbon monoxide on conventionally produced catalysts (on an equal surface area, i.e., 0.3 m^2). Such catalysts are, for example, the copper-impregnated polycrystalline Cu/CeO_2 and Cu/TiO_2, as well as the combustion catalyst Pt/CeO_2, generally considered highly active and commonly used. All three show higher light-off temperatures than the majority of our nanostructured CuO_x/CeO_2 composite catalysts, with the 50% conversion level at 178, 226, and 183°C (Fig. 7a, Table 1), respectively. Thus, IGC-produced CuO_x/CeO_2 catalysts can be classified as an exceptionally active group of catalysts, especially for the combustion of carbon monoxide.

4. DISCUSSION

4.1. X-Ray Photoelectron Spectroscopy

By using impregnation methods the distribution of copper is mainly restricted to the particle surface. The aggregation of well-dispersed surface clusters into larger bulk particles of copper will, therefore, occur at relatively low concentrations (15, 55). On the other hand, nanocrystalline aggregates of CeO_2 produced by IGC are capable of stabilizing a very high portion of copper species before particles of bulk CuO will emerge. In fact, no maximum dispersion limit of copper over ceria was observed (37).

For all catalysts, the XPS measurements show reduced phases of both cerium (<20% reduction as compared to the bulk CeO_2 reference) and copper (<50% reduction as compared to the bulk CuO reference) (Table 2). Reduced copper species can be stabilized on the surface of the ceria crystallites, without causing a detectable angular lineshift in HED (significant of a solid solution). As expected, the degree of reduction appears to be somewhat enhanced due to the photoreduction in the spectrometer, since the reduction, as recorded by XPS, is considerably greater than that detected of the bulk by HED or by XAS (Table 3).The surfaces of nanocrystalline ceria, however, are expected to show a greater reducibility than bulk ceria (56–59).

After thermal activation, the Cu 2p XP spectra become more similar to those of the fully oxidized bulk CuO, indicating that the copper is being oxidized during the induction (Table 2). In addition, an increased copper signal is obtained for the activated catalysts. This shows that the finely dispersed copper species are migrating toward the surface of the particle aggregates during the thermal activation process. This finding is supported by previous investigations (15, 28, 55). Dependent on the total copper concentration and heating temperature, the copper species coalesce into clusters at the particle's surface. Upon exposure to ambient air, these superficial nanoclusters are likely to be oxidized into Cu(II), with oxygen originating either from the ceria lattice or from the gas phase (53). Thus, the Cu 2p spectra would show a more oxidized copper oxide phase, differing from the phase that prevails during the catalytic surface reactions. Since the migration of copper toward the surface is accompanied by a reduction of the ceria surface (Table 2), the ceria lattice is expected to be the source of oxygen. It should be pointed out, however, that copper ions with a lower coordination environment (e.g., at the surface) also should exhibit increased Cu 2p-satellite signals, i.e.,

showing an apparent oxidation of the copper (60). These kinds of nanostructure evolutions of the catalyst provide for an enhanced copper surface dispersion that gives improved catalytic activity and durability of these nanocomposite materials.

We have previously suggested (37) that a similar evolution phenomenon is occurring already at the collective cold finger during the post-oxidation of metallic nanoparticles. The sequential oxidation of Ce followed by Cu, with an accompanying lattice expansion, may promote the efficient dispersion of the copper on ceria already during the IGC synthesis of the particles.

4.2. High-Energy Diffraction

By reducing the CeO_2 unit cell, one approaches the dimension of the *C*-type sesquioxide Ce_2O_3 (30, 61), which is essentially an expanded fluorite structure (<3.7%), with a $2 \times 2 \times 2$ supercell. Although the sesquioxide is rarely observed (62), highly oxygen-deficient CeO_{2-x} is often reported (up to 74%) (25–27, 62, 63). The HED measurements showed a small average unit cell expansion of CeO_2, which indicates a slightly nonstoichiometric lattice (oxygen-deficient) (37). The detected unit cell expansion (ca. 0.08%), according to Vegard's law (64), would correspond to the chemical composition $CeO_{1.989}$, i.e., a total bulk reduction of 2.2%. It should be kept in mind, however, that the expansion of the unit cell could be balanced, at least partly, by an inclusion of copper ions in the lattice that causes a simultaneous unit cell contraction.

When diffraction lines of copper phases are detected (>30% Cu), we found no apparent systematic correlation to the total copper content in the sample. Thus, a major part of the copper is still highly disordered according to the HED and EXAFS results (or dispersed according to HREM), even after the detection of a CuO phase, which agrees with the results reported by Ying and colleagues (25, 26, 36) and others (15, 16, 35, 65).

Generally poor crystallinity of the ceria phase was detected. We have previously shown a clear correlation between the crystallinity and the particle morphology as observed by HREM (37). Poorly crystalline ceria by itself has been reported to be more active for the combustion of carbon monoxide than well-crystallized ceria (40, 66).

4.3. X-Ray Absorption Spectroscopy

XANES. The pre-edges in our catalyst samples are relatively intense and correspond well to the energy of the linear 2-coordinate copper (8982 eV) (Fig. 4). It is clear that in our case the major part of Cu(I) species has the same coordination as the Cu_2O reference compound, or alternatively, a 3-fold planar coordination. If we consider that the Cu(I) species in the catalysts have mostly the same coordination as in the reference compound Cu_2O, the relative amount of Cu(I) species in the CuO_x/CeO_2 composites can be estimated from XANES data (51). To begin with, the spectrum of the normalized CuO reference sample (containing only Cu(II)) must be subtracted from the spectra of the different catalysts. Thereafter, by measuring the height of the pre-edge peak relative to the height corresponding to the subtracted reference compound Cu_2O (containing only Cu(I) species), a relative evaluation of the ratio of the amounts of Cu(I) and Cu(II) species can be achieved. For the three fresh CuO_x/CeO_2 catalysts A4, C1, and B4, the calculation gives respectively a relative ratio Cu(I)/Cu(II) corresponding to 36, 27, and 16% Cu(I). For the same samples, but in their activated form, the ratio was always found to be less than 5%, indicating that the major part of the Cu(I) was oxidized to Cu(II) during the process.

This pre-edge, corresponding to the 1s–4p transition of the Cu(I) species, has never been observed from Cu(II) (51). This feature is specific to Cu(I) species and can be used to identify them qualitatively and quantitatively in a sample. Moreover, a distinction can be made between the coordination of these ions according to the position and the relative intensity of this pre-edge peak. Cu(I) compounds with linear 2-coordinates exhibit a split 1s–4p transition (51). The main transition corresponds to the dipole allowed transition from 1s to the doubly degenerate $4p_{x,y}$ final state and is characterized by a sharp and intense pre-edge absorption peak at about 8982 eV on the XANES spectrum. In the case of a planar 3-coordinate configuration this pre-edge peak would correspond to the 1s–$4p_x$ transition. For the 4-coordinate tetrahedral structure, assigned to Cu(II), the $4p_{xyz}$ orbitals degenerate, but shifted to higher energies than for the two previous coordinations. The peak corresponding to this transition is unique, shifted to higher energy (around 8985 eV), and exhibits a reduced intensity compared to the linear and planar coordinations (51).

EXAFS. The *A4 catalyst*, showing a much smaller Cu–O distance (1.89 Å) and higher coordination number (ca. 3) of the copper–copper shell, is very different from the two other examined catalysts. The copper seems to form larger clusters than in the B4 and C1 catalysts featuring higher copper content. The presence of a well-defined oxygen shell at 2.479 Å could mean that the Cu(II) species in this catalyst have a well-defined, but distorted octahedral coordination. This could be linked to the presence of larger and better ordered copper clusters.

In good agreement with the XANES results, the fresh A4 catalyst presents the highest proportion of Cu(I) species (36%) of the three examined catalysts. The presence of reduced copper ions is known to decrease the apparent activation energy and enhance the strength of adsorption for CO (53). This could explain the higher low-temperature catalytic activity for the A4 catalyst (Fig. 7b). The Cu(I) species show a structure closely related to the linear 2-coordinate

structure as in the Cu_2O (52) reference sample. Because EXAFS only see the average of the environment around all copper ions, the presence of this low-coordinated copper could in turn explain the small coordination number of the first oxygen shell (3.5). Moreover, the linear coordination is certainly associated with shorter distances (1.846 Å in Cu_2O) also explaining the decrease in the average Cu–O distances of the first coordination shell. After the activation process, the distance of the first shell is dramatically increased from 1.89 to 1.94 Å; also the coordination number increases slightly. The second oxygen shell at 2.48 Å has disappeared in the activated sample, while the coordination number and the distance of the third shell, corresponding to copper, have also decreased. In its activated form the A4 sample presents a coordination similar to that of tetrahedral Cu(II). This extensive structural evolution in the A4 catalyst can be monitored by a large shift of the light-off temperature during the thermal activation (Table 3).

The *B4 sample* shows minor structural changes as it is activated. Both the fresh and activated forms could be fitted with four oxygen atoms at 1.924 Å and two oxygen atoms at 2.48 Å. This is similar to the Cu(II) ions in CuO, which exhibit a typical [4 + 2] Jahn–Teller-distorted coordination by six oxygen atoms (1.96 Å × 4 and 2.78 Å × 2) (52). However, the large Debye–Waller factors (Table 4) associated with the second oxygen shell signify certainly that this distorted octahedral coordination is highly disordered or could even be a mixture of tetrahedral and octahedral coordinations. The proportion of Cu(I) species in the fresh sample was shown by XANES to be the lowest (16%) of all the catalysts. Therefore, the activation process of the B4 catalyst is expected to have a minor impact on the structure. This may, thus, explain the relatively smaller light-off temperature shift that was recorded for B4 compared to A4 and C1 catalysts.

The EXAFS results of the *C1 catalyst* (the richest in copper), for the same reasons as those in the B4 case, show that the activation process has only slightly increased the bond distance of the first Cu–O shell from 1.924 to 1.935 Å, as well as the coordination number of the Cu–Cu shell. In contrast to the B4 sample, the presence of a second oxygen shell in this case did not improve the quality of the fit significantly. The coordination of copper in this sample is mostly tetrahedral.

In summary, the X-ray absorption spectroscopy study shows that the copper is present in a very dispersed and amorphous form with a mixture of Cu(I) and Cu(II) species in a ratio varying from 36% in the fresh samples to less than 5% in the activated samples. The major part of Cu(I) is likely to adopt a two-fold linear coordination as in the model compound Cu_2O, or possibly a mixture of linear and planar coordination. In general, the Cu(II) species present a tetrahedral coordination, and/or a highly distorted octahedral coordination as in the reference compound CuO, or a mixture of the two coordinations. Opposed to the other samples, the fresh A4 catalyst displays a very well-defined distorted octahedral coordination.

In all the activated catalysts the copper species were found to be in a generally lower coordination. Thus, this suggests that the copper ions migrate out from the CeO_2 crystallite aggregates toward the surface, where they reach a lower coordination environment. This observation is consistent with our XPS measurements, as well as with the results of Liu *et al.* (16). Once the copper clusters are exposed on the surface, they may more easily participate in redox mechanisms between Cu(II) and Cu(I), or even to metallic Cu(0) directly (54). In addition, if the copper species are part of a highly disordered environment, they are more easily reduced than crystalline copper aggregates (19). For the high-temperature shift catalyst (Cu–Fe–Cr) (67), and catalysts used for methanol synthesis ($CeCu_2$, Cu/ZnO) (13, 68, 69), for example, it has been shown by *in situ* EXAFS measurements that superficial metallic clusters of copper directly (or indirectly by alloy formation) may be responsible for the enhanced catalytic activity. However, we found no clear evidence in the present work that Cu(0) could be an active species in the CuO_x/CeO_2 catalysts.

4.4. Carbon Monoxide Oxidation

Catalytic activity. The catalysts in category B (5–25% Cu) show the best catalytic properties (Fig. 6). Keeping in mind that the composite catalysts in this group consist of several tightly interfaced CeO_2 nanocrystals, which form an apparent solid matrix of rounded aggregates (Fig. 2), we suggest that the copper, which was significantly detected neither by HREM nor by HED, is amorphously dispersed over the ceria crystallites as is indicated by EXAFS. In addition, XPS showed that for the 5–15% Cu range the dispersed copper species are preferentially located at the surface of the CeO_2 nanocrystals (37). These facts would increase the total synergistic contact area between the CuO_x and CeO_2, as well as the number of adsorption sites, which contribute to the enhanced catalytic activity for the group B catalysts.

Increasing the copper content above 30% (group C) does not result in an improved conversion rate. We postulate that the reason for this is twofold, namely (i) the formation of crust structures (37) and (ii) the formation of bulk tenorite. The formation of crust structures (i) is favored at concentrations between 30 and 70% copper. The freshly prepared samples expose shells of crystalline CeO_2 with a core of metallic copper captured inside (37, 70). This kind of morphology would initially (for fresh samples) exhibit a lower catalytic activity, since CeO_2 is predominantly exposed on the outside of the nanocomposites. However, the conversion rate increases gradually during the induction period in the oxidizing atmosphere. This suggests that the encapsulated copper slowly migrates toward the outside,

oxidizes over/between the CeO_2 crystallites, and contributes to the extreme copper dispersion. In fact, the fresh catalyst C1 (Fig. 3) with a pronounced crust morphology exhibits a fairly high T_{50} value, but the lowest T_{50} value of all catalysts after activation, i.e., a large T_{50} shift (Fig. 7b). For the latter case (ii) above 30% Cu, particles of bulk CuO (tenorite) are formed already during the IGC synthesis, but with a preserved high copper dispersion (37). At elevated temperatures, e.g., during the thermal activation, the highly dispersed copper species, or atomic-sized clusters, are driven to the surface of the ceria aggregates, as shown by XPS and XAS (Tables 2 and 4), where they in *excess* may form larger clusters or particles of CuO that can, in part cover the active catalyst surface. This would reduce the catalytic activity, since bulk CuO is known to be an insulator and contribute very little to the total active area (13, 15, 16, 53). It has also been suggested that the monoclinic distortion of the fully oxidized tenorite CuO phase destroys an epitaxial relationship to the ceria support, preventing an effective transfer of oxygen, and hence, showing lower catalytic activity (23).

The small improvement in the conversion rate observed at approximately 80% Cu (Fig. 6) could be an effect of a reversed morphology compared to that of the low-copper-content catalysts; i.e., ceria crystallites are finely dispersed over a copper oxide support (37). This would increase the active surface area, but without a serious loss of the favourable synergistic effects. For even higher copper content (>80% Cu), however, the synergism is inevitably greatly reduced. It is thus likely that the active surface will be rapidly fouled by coke formation, due to the slower oxygen regeneration capability resulting in a reduced lifetime of the catalyst.

In summary, the CuO_x/CeO_2 catalyst can sustain a high catalytic activity as long as a high surface concentration of copper can be maintained. A loss of the superficial copper species can originate from (i) structural encapsulation (discrimination) by CeO_2, (ii) the formation and blocking of active surface by bulk CuO, or (iii) the loss of copper dispersion by coalescence or sintering.

Thermal activation. The induction process, as detected by the change of the light-off temperature curve, was shown to vary considerably from one catalyst to the other (Fig. 7b). The difference in behavior during activation of the catalysts can be ascribed to various reasons: (a) The structure, or morphology, may rearrange and change the properties of the surface facets upon heating, possibly by introducing new adsorption sites and invoking catalytic anisotropy (23, 71) or (b) the elimination of precursors or impurities from the preparation process, such as water. The latter explanation has been rejected for the following reasons: The gas-phase synthesis of pure metals is a very clean process, and adsorbed water and hydroxyl species were not detected significantly by FT–IR measurements on fresh catalysts (37). The first explanation is therefore the most likely considering the sample-specific nanostructured morphology of the CuO_x/CeO_2 catalysts as detected by HREM, XAS, and HED. At elevated temperatures the enhancement of the ionic mobility, or migration, has been reported to reconstruct or relax the surfaces of CeO_2 (56, 57). Stronger relaxations appear in general in those surfaces which are less stable because of a less compact character and a lower coordinative saturation of the surface ions. Highly disordered and nanocrystalline catalyst composites, as opposed to highly X-ray crystalline catalysts, would thus undergo a more extensive restructuring process during a thermal treatment (Fig. 9). According to the XAS measurements the oxidation of Cu(I) to Cu(II), upon thermal activation, changes the coordination environment inflicting structural rearrangements. Since no change in morphology was observed by HREM or HED between fresh and activated catalysts, the structural rearrangements must be of a diminutive magnitude, which cannot unambiguously be resolved .

In general, an increased amount of reduced copper species increases the activity and reduces the light-off temperature (Table 3). Initially, when the surface is almost completely covered with adsorbed oxygen, the CO conversion rate depends not only on the partial pressure of CO, but also on the available number of adsorption sites (16, 24, 54, 72). Once the light-off temperature is reached, CO is rapidly converted to CO_2. Hence, independent of activity, a steep light-off curve shape (small ΔT_{10-90}; e.g., the A4, B4, C1) would designate a high concentration of active copper species. Conversely, samples showing wider light-off curve shapes would expose relatively less active copper species at the catalyst surface (e.g., A3, B3; Fig. 7a, Table 3). Liu *et al.* (55) and Hočevar *et al.* (18) have shown that smaller crystals of CuO detectable by X rays can disappear upon use of the catalyst, or by heating. Their findings indicate that the dispersion of copper can be enhanced if the conditions are favorable. Hence, for the CuO_x/CeO_2 catalysts, we suggest that copper species/ions migrate along the boundaries of the nanocrystalline aggregates and amorphous matrix toward the surface. The catalytic activity is enhanced by the increasing number of active adsorption sites for carbon monoxide, which is observed as a change in light-off curve shape showing steeper slopes at lower temperatures (Fig. 7b).

The wide variation in induction processes between different catalysts can be clarified in terms of the degree of copper reduction and the X-ray crystallinity, which are both closely correlated to the particle morphology as observed by HREM (37). Less X-ray crystalline catalysts and seemingly amorphous catalysts (e.g., A4, B4) expose a higher portion of high-energy surfaces of ceria (e.g., {100}). Such surfaces may efficiently stabilize reduced copper species,

as determined by XANES, and provide a strong synergistic interaction at low temperatures. On the other hand, a catalyst consisting of larger and well-defined CeO_2 crystals clearly shows a more crystalline character, which is supported by the HED crystallinity factor (e.g., A3, B3, Table 3). The less Cu(I) species and the more crystalline the catalysts are, the faster they reach their maximum activity; i.e., they have a short induction period (Fig. 9). This suggests that the higher portion of low-energy surfaces of ceria (e.g., {111}) in these kinds of catalysts cannot adequately stabilize reduced copper species and impedes the dispersion of copper. Instead, larger surface clusters of Cu(II) oxide will be formed. Moreover, this would explain why the less crystalline catalyst B3, compared to catalyst B4, exhibits an initially higher activity and a smaller T_{50} shift (Table 3, Figs. 7a and 7b). Thus, the crystallinity factor and the portion of Cu(I) species as determined by XANES can be used to explain and partly quantify the processes occurring during the induction of the catalyst.

CONCLUSIONS

Nonstoichiometric CuO_x/CeO_2 composite catalysts, produced by inert gas condensation, show a varying nanostructured morphology that is strongly dependent on the copper content. These variations can dramatically influence the catalytic activity for the oxidation of carbon monoxide. The main chemical factors that control the activity are (i) the nanostructured morphology, (ii) the X-ray crystallinity, and (iii) the valence and dispersion of copper species at the surface. These three factors can be tailored during the IGC synthesis, but they will also change during the thermal activation.

X-ray absorption spectroscopy showed that copper was present as a mixture of Cu(I) and Cu(II) species ranging from ca. 36% for fresh catalysts to less than 5% for the activated catalysts. Upon thermal activation, i.e., induction, copper species migrate toward the surface where they create new superficial active copper species/clusters, which in turn introduce additional vacancies (by reduction) at the CeO_2 surface. The coordination of Cu(I) was found to be mostly linear 2-coordinate as in the model compound Cu_2O, or alternatively 3-coordinate planar, while Cu(II) was found to present a mixture of tetrahedral and highly distorted octahedral coordinations. Especially the catalysts that show a very amorphous character of the ceria phase exhibit initially a high portion of Cu(I) species with an extremely high dispersion of copper. These catalysts, compared to the more crystalline catalysts, undergo extensive structural rearrangements during the thermal activation. This kind of nanostructure evolution is observed as a shift in the light-off temperature.

The broad copper concentration range (5–30%) for which these nanocomposites exhibit the highest catalytic activity can be explained by the variations in nanosized morphology and X-ray crystallinity. A crust morphology (most frequently observed between 25–70% Cu content), which initially encapsulates the copper, may result in an enhancement of the copper dispersion at elevated temperatures. A too-high copper content (70–100%) reduces the synergistic effects and favors the formation of larger bulk CuO clusters, which reduces the active surface area.

We suggest that the superior catalytic activity of the CuO_x/CeO_2 catalyst system in oxidizing carbon monoxide at low temperatures can be explained by a quick reversible redox process of superficial Cu(I)/(II) couples in strong synergistic interaction with the nanocrystalline ceria support. The most X-ray amorphous catalysts expose surfaces with enhanced reducibility of Ce^{4+} to Ce^{3+}, which promote the ability of the copper ions to adopt different oxidation states and supply oxygen.

ACKNOWLEDGMENTS

Support from the Sweden–Japan foundation, the Swedish Natural Science Research Council, and the EU-supported TMR network CLUPOS (Contract Number FMRX-CT98-0177) is gratefully acknowledged. The ESRF facility in Grenoble, France, is acknowledged for the XAS experiments at BM29. Dr. Nakayama and Professor Niihara at the Institute of Scientific and Industrial Research (ISIR), Osaka University, Japan, are acknowledged for providing the IGC apparatus and for a fruitful cooperation.

REFERENCES

1. Inoue, T., Setoguchi, T., Eguchi, K., and Arai, H., *Solid State Ionics* **34**, 285 (1989).
2. Park, S., Vohs, J. M., and Gorte, R. J., *Nature* **404**, 265 (2000).
3. Lavrencic, S. U., Orel, B., Grabec, I., Ogrovec, B., and Kalcher, K., *Sol. Energy Mater.* **31**, 171 (1993).
4. Lampe, U., Gerblinger, J., and Meixner, H., *Sens. Actuators, B* **7**, 787 (1992).
5. Trovarelli, A., *Catal. Rev.* **38**, 439 (1996).
6. Trovarelli, A., de Leitenburg, C., Boaro, M., and Dolcetti, G., *Catal. Today* **50**, 353 (1999).
7. Bunluesin, T., Gorte, R. J., and Graham, G. W., *Appl. Catal. B* **14**, 105 (1997).
8. Logan, A. D., and Shelef, M., *J. Mater. Res.* **9**, 468 (1994).
9. Bunluesin, T., Putna, E. S., and Gorte, R., *J. Catal. Lett.* **41**, 1 (1996).
10. Johansson, S., Wong, K., Zhdanov, V. P., and Kasemo, B., *J. Vac. Sci. Technol. A* **17**(1), 297 (1999).
11. Holmgren, A., Ph.D. thesis, Chalmers University of Technology, Sweden, 1998.
12. Bernal, S., Calvino, J. J., Cauqui, M. A., Pérez Omil, J. A., Pintado, J. M., and Rodríguez-Izquierdo, J. M., *Appl. Catal. B* **16**, 127 (1998).
13. Shaw, E. A., Rayment, T., Walker, A. P., Lambert, R. M., Gauntlett, T., Oldman, R. J., and Dent, A., *Catal. Today* **9**, 197 (1991).
14. Lamonier, C., Bennani, A., D'Huysser, A., Aboukaïs, A., and Wrobel, G., *J. Chem. Soc., Faraday Trans.* **92**, 131 (1996).
15. Liu, W., and Flytzani-Stephanopoulos, M., *J. Catal.* **153**, 304 (1995).
16. Liu, W., and Flytzani-Stephanopoulos, M., *J. Catal.* **153**, 317 (1995).
17. Hočevar, S., Batista, J., and Levec, J., *J. Catal.* **184**, 39 (1999).
18. Hočevar, S., Krasovec, U. O., Orel, B., Arico, A. S., and Kim, H., *Appl. Catal. B* **28**, 113 (2000).

19. Harrison, P. G., Ball, I. K., Azalee, W., Daniell, W., and Goldfarb, D., *Chem. Mater.* **12**(12), 3715 (2000).
20. Larsson, P.-O., and Andersson, A., *Appl. Catal. B* **24**, 175 (2000).
21. Zhu, T., Kundakovic, L., Dreher, A., and Flytzani-Stephanopoulos, M., *Catal. Today* **50**, 381 (1999).
22. Yue, L., Qi, L., and Flytzani-Stephanopoulos, M., *Appl. Catal. B* **27**, 179 (2000).
23. Skårman, B., Wallenberg, L. R., Larsson, P.-O., Andersson, A., Bovin, J.-O., Jacobsen, S. N., and Helmersson, U., *J. Catal.* **181**, 6 (1999).
24. Satterfield, C. N., *in* "Heterogeneous Catalysis in Industrial Practice," 2nd ed. Krieger, Malabar, FL, 1996.
25. Ying, J. Y., Tschöpe, A., and Levin, D., *Nanostruct. Mater.* **6**, 237 (1995).
26. Ying, J. Y., and Tschöpe, A., *The Chem. Eng. J.* **64**, 225 (1996).
27. Guillou, N., Nistor, L. C., Fuess, H., and Hahn, H., *Nanostruct. Mater.* **8**, 545 (1997).
28. Tschöpe, A., Liu, W., Flytzani-Stephanopoulos, M., and Ying, J. Y., *J. Catal.* **157**, 42 (1995).
29. Lavik, E. B., and Chiang, Y.-M., *Mat. Res. Soc. Symp. Proc.* **457**, 63 (1997).
30. Wallenberg, L. R., Withers, R. L., Bevan, D. J. M., Thompson, J. G., and Hyde, B. G., *J. Less Com. Met.* **156**, 1 (1989).
31. Palmqvist, A. E. C., Wirde, M., Gelius, U., and Muhammed, M., *Nanostruct. Mater.* **11**, 995 (1999).
32. Mamontov, E., Egami, T., Brezny, R., Koranne, M., and Tyagi, S., *J. Phys. Chem. B* **104**, 11,110 (2000).
33. Fernández-García, M., Rebollo, G. E., Ruiz, A. G., Conesa, J. C., and Soria, J., *J. Catal.* **172**, 146 (1997).
34. Terrible, D., Trovarelli, A., Leitenburg de, C., Primavera, A., and Dolcetti, G., *Catal. Today* **47**, 133 (1999).
35. Jiang, X., Lu, G., Zhou, R., Mao, J., Chen, Y., and Zheng, X., *Appl. Surf. Sci.* **173**, 208 (2001).
36. Tschöpe, A., Ying, J. Y., and Chiang, Y.-M., *Mater. Sci. Eng. A* **204**, 267 (1995).
37. Skårman, B., Nakayama, T., Grandjean, D., Benfield, R. E., Olsson, E., Niihara, K., and Wallenberg, L. R., *Chem. Mater.*, in press.
38. Williams, F. W., Woods, F. J., and Umstead, M. E., *J. Chromatog. Sci.* **10**, 570 (1972).
39. Larsson, P.-O., Andersson, A., Wallenberg, L. R., and Svensson, B., *J. Catal.* **163**, 279 (1996).
40. Park, P. W., and Ledford, J. S., *Langmuir* **12**, 1794 (1996).
41. http://www.esrf.fr/exp_facilities/ID15B/home/id15home.html.
42. Scherrer, P., *Gött. Nachr.* **2**, 98 (1918).
43. http://www.esrf.fr/exp_facilities/BM29/bm29control.html.
44. Binstead, N., Campbell, J. W., Gurman, S. J., and Stephenson, P. C., "EXAFS Analysis Programs." Daresbury Laboratory, Warrington, 1991.
45. Chusuei, C. C., Brookshier, M. A., and Goodman, D. W., *Langmuir* **15**, 2806 (1999).
46. Frost, D. C., Ishitani, A., and McDowell, C. A., *Mol. Phys.* **24**, 861 (1972).
47. Evans, S., *J. Chem. Soc. Faraday Trans. II* **71**, 1044 (1975).
48. Bensalem, A., Bozon-Verduraz, F., Delamar, M., and Bugli, G., *Appl. Catal. A* **121**, 81 (1995).
49. Shyu, J. Z., Weber, W. H., and Gandhi, H. S., *J. Phys. Chem.* **92**, 4964 (1988).
50. Larsson, P.-O., and Andersson, A., *J. Catal.* **179**, 72 (1998).
51. Kau, L.-S., Spira-Solomon, J., Penner-Hahn, J. E., Hodgson, K. O., and Solomon, E. I., *J. Am. Chem. Soc.* **109**, 6433 (1987).
52. Åsbrink, S., and Lorrby, L. J., *Acta Crystallogr. B* **26**, 8 (1970).
53. Jernigan, G. G., and Somorjai, G. A., *J. Catal.* **147**, 567 (1994), doi:10, 1006/jcat.1994.1173.
54. Nagase, K., Zheng, Y., Kodama, Y., and Kakuta, J., *J. Catal.* **187**, 123 (1999).
55. Liu, W., Sarofim, A. F., and Flytzani-Stephanopoulos, M., *Appl. Catal. B* **4**, 167 (1994).
56. Conesa, J. C., *Surf. Sci.* **339**, 337 (1995).
57. Baudin, M., Ph.D. thesis, Uppsala University, Uppsala, Sweden, 2000.
58. Tsunekawa, S., Kasuya, A., and Fukuda, T., *Surf. Sci.* **427**, L437 (2000).
59. Putna, E. S., Vohs, J. M., and Gorte, R. J., *J. Phys. Chem.* **100**, 17,862 (1996).
60. Dong, L., Jin, Y., and Chen, Y., *Sci. China B* **40**, 24 (1997).
61. Withers, R. L., Thompson, J. G., Gabbitas, N., Wallenberg, L. R., and Welberry, T. R., *J. Solid-State Chem.* **120**, 290 (1995).
62. Perrichon, V., Laachir, A., Bergeret, G., Fréty, R., Tournayan, L., and Touret, O., *J. Chem. Soc. Faraday Trans.* **90**, 773 (1994).
63. Tsunekawa, S., Sivamohan, R., Ito, S., Kasuya, A., and Fukuda, T., *Nanostruct. Mater.* **11**, 141 (1999).
64. Vegard, L., and Dale, H., *Z. Krist.* **67**, 148 (1928).
65. Daniell, W., Lloyd, N. C., Bailey, C., and Harrison, P. G., *J. De Phys. IV* **7**, 963 (1997).
66. Craciun, R., *Solid State Ionics* **110**, 83 (1998).
67. Kappen, P., Grunwaldt, J.-D., Hammershöi, B. S., Tröger, L., and Clausen, B. S., *J. Catal.* **198**, 56 (2001).
68. Clausen, B. S., and Topsøe, H., *Catal. Today* **9**, 189 (1991).
69. Grunwaldt, J.-D., Molenbroek, A. M., Topsoe, N.-Y., Topsoe, H., and Clausen, B. S., *J. Catal.* **194**, 452 (2000).
70. Skårman, B., Nakayama, T., Niihara, K., and Wallenberg, L. R., *Microsc. Microanal. Proc.* **7**, 1074 (2001).
71. Stubenrauch, J., and Vohs, J. M., *J. Catal.* **159**, 50 (1996).
72. Tanaka, K., and Blyholder, G., *J. Phys. Chem.* **75**, 1807 (1971).